International Journal of Solids and Structures 72 (2015) 26–37

Contents lists available at ScienceDirect

International Journal of Solids and Structures

journal homepage: www.elsevier.com/locate/ijsolstr

A linear sampling method for detecting fluctuations of the wavefield in an elastic half-space

Terumi Touhei *, Yasufumi Fukushiro, Takumi Tanaka

Dept. of Civil Engineering, Tokyo University of Science, 2641 Yamazaki, Noda 278-8510, Japan

ARTICLE INFO

Article history:
Received 5 August 2014
Received in revised form 20 April 2015
Available online 16 July 2015

Keywords:
Linear sampling method
Solvability index
Inverse scattering problem
Elastic half-space
Fluctuation of the wavefield
Projection theorem of a Hilbert space
Singular value decomposition

ABSTRACT

A linear sampling method for an elastic half-space is developed to reconstruct fluctuations in the wavefield. The starting point of the formulation is the near-field equation that was also used by Baganas et al. (2006). Instead of examining the norm of the solution of the near-field equation, we define a solvability index in order to obtain the spatial distribution of the amplitude of the solvability index and thus describe the location of the fluctuations. A numerical method for the evaluation of the index is also provided for a simplified algorithm; this method is based on a projection theorem for a Hilbert space and a singular value decomposition. Numerical calculations were performed, and the results validated the efficiency of the proposed method for reconstructing the fluctuations of a wavefield.

1. Introduction

Inverse scattering analysis has a long history due to its inherent interest, as well as its applications in the fields of geophysical exploration, site characterization, medical imaging, nondestructive testing, and many other areas. Colton and Kress (1998) surveyed and reported a vast number of articles on inverse scattering analyses of acoustic and electromagnetic wave propagation. During the past ten years, many significant articles in this field have been published. For example, Guzina et al. (2003) used the regularized boundary integral equation method to solve the problem of mapping underground cavities. Pelekanos et al. (2004) presented a contrast source inversion method in a 2D elastic wavefield. Campman et al. (2006) formulated a method to estimate the wavefield that would have been measured if there were no near-receiver heterogeneities. Gélis et al. (2007) carried out a 2D full elastic waveform inversion using the Born and Rytov approximations. Romdhane et al. (2011) applied a 2D full waveform inversion to a shallow structure with complex topography. The authors' research group also presented a fast method for solving a volume integral equation (Touhei, 2009, 2011; Touhei et al., 2009) and applied it to an inverse scattering analysis (Touhei et al., 2014).

Among the various methods for the inverse scattering analysis, a linear sampling method, presented by Colton and Kirsch (1996), reconstructs the supports of the scatterers by tracing the norm of the solution of the far-field equation without information about the type of boundary conditions on the scatterers. A factorization method, presented by Kirsch (2011), reconstructs the support of scatterers by decomposing the far-field operator and examining its range, instead of solving the far-field equation. Colton and Kirsch (1996) used a linear sampling method with a 2D scalar Helmholtz equation for the far-field equation, but Fata and Guzina (2004) proposed a linear sampling method that uses the near-field equation. They provided the mathematical details of the near-field equation and then used it to analyze the reconstruction of cavities embedded in a 3D elastic half-space. Baganas et al. (2006) extended the method of the near-field equation to the inverse transmission problem of an elastic half-space. Guzina and Madyarov (2007) used a linear sampling method to reconstruct scatterers in piecewise-homogeneous domains. The authors' research group also used a linear sampling approach to evaluate the location and spatial spread of the fluctuations, and we ensured the accuracy of the reconstructed amplitudes by using the fast volume integral equation method (Touhei et al., 2014). In that paper, we presented only a brief outline of our method and its results, and a detailed description of the method and numerical results were left as an area of future work.

The purpose of the present article is to provide a detailed mathematical description of our method for evaluating the location and spatial spread of fluctuations in an elastic half-space and to provide numerical examples. The inversion equation used in this article is

* Corresponding author.
E-mail address: touhei@rs.noda.tus.ac.jp (T. Touhei).

http://dx.doi.org/10.1016/j.ijsolstr.2015.07.008
0020-7683/

the near-field equation, which was also used by Fata and Guzina (2004) and Baganas et al. (2006). Instead of using the divergence properties of the near-field equation, we developed a solvability index for the equation; the spatial distribution of the fluctuations corresponds to the spatial distribution of the amplitude of the solvability index.

The organization of this paper is as follows.

In order to develop the concept of the solvability index of the near-field equation, we review the basic results of Fata and Guzina (2004) and Baganas et al. (2006), and we employ a method for the factorization of the operator (Kirsch, 2011). Using these results, we present the mathematical properties of the solvability index. Next, we present a method for evaluating the solvability index; this method is based on a projection theorem for a Hilbert space. After providing the formulation for the inverse scattering analysis, several numerical examples are presented to show the accuracy of this method. The intended application of the present method is to detect the spatial spreads of localized fluctuations in homogeneous background structures with high-velocity waves; an example of this is S waves with a velocity of 1 km/s.

2. Theoretical Formulation

2.1. Definition of the problem and the basic equation

Fig. 1 shows the wave problem defined in this article. The wavefield is a 3D elastic half-space in which there are fluctuations in contrast to a homogeneous background structure. On the free surface of the wavefield, there are both source and observation surfaces, which are denoted by Γ_1 and Γ_2, respectively. Distributed loads are applied to Γ_1 so that incident waves are scattered, and these are observed at Γ_2. The problem defined in this article is as follows:

Definition of the problem *We consider using information from the distributed loads at* Γ_1 *and the observed scattered waves at* Γ_2 to reconstruct the spatial spread and the location of the fluctuations.

As shown in Fig. 1, a Cartesian coordinate system is employed to express the wavefield; the vertical axis is denoted by x_3. A spatial point in the wavefield is expressed as

$$x = (x_1, x_2, x_3) \in \mathbb{R}^2 \times \mathbb{R}_+ = \mathbb{R}^3_+ \tag{1}$$

where the subscript index indicates the component of the Cartesian coordinate system. The free boundary of the elastic half-space, denoted by B, is at $x_3 = 0$. In the following, the summation convention is applied to the subscript indexes describing the Cartesian coordinate system. Using the summation convention, the scalar product of wavefunctions is defined as follows:

$$(\varphi_i,\ \psi_i)_{L_2(\Gamma_k)} = \int_{\Gamma_k} \varphi_i^*(x)\psi_i(x)\mathrm{d}\Gamma_k(x), \quad \varphi_i, \psi_i \in L_2(\Gamma_k) \tag{2}$$

where k takes 1 or 2. The L_2 norm is defined as the scalar product, which is represented in the following form:

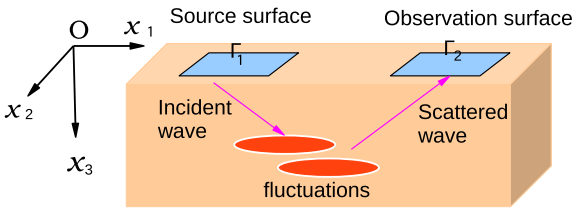

Fig. 1. Wave problem considered in this article.

$$\|\varphi_i\|^2_{L_2(\Gamma_k)} = (\varphi_i,\ \varphi_i)_{L_2(\Gamma_k)} \tag{3}$$

The Lamé constants and the mass density that characterize the wavefield are expressed as

$$\begin{aligned} \lambda(x) &= \lambda_0 + \tilde{\lambda}(x) \\ \mu(x) &= \mu_0 + \tilde{\mu}(x) \\ \rho(x) &= \rho_0 + \tilde{\rho}(x), \quad (x \in \mathbb{R}^3_+) \end{aligned} \tag{4}$$

where λ_0, μ_0 are the background Lamé constants, and ρ_0 is the mass density. Their respective fluctuations are $\tilde{\lambda}$, $\tilde{\mu}$, and $\tilde{\rho}$. The fluctuations are assumed to be characterized as

$$\tilde{\lambda}(x),\ \tilde{\mu}(x),\ \tilde{\rho}(x) \in C^1_0(\mathbb{R}^3_+) \tag{5}$$

We define the support of the fluctuations E such that

$$E = \mathrm{supp}\ \tilde{\lambda}(x) \cup \mathrm{supp}\ \tilde{\mu}(x) \cup \mathrm{supp}\ \tilde{\rho}(x) \tag{6}$$

and we let ∂E express the boundary of E. Namely, E can be expressed by

$$E = E^o \cup \partial E \tag{7}$$

where E^o is the set of internal points of E. In addition, we assume that the complementary set of E, denoted by E^c, is connected. In addition, the free boundary B and the fluctuated regions are disjoint:

$$E \cap B = \emptyset \tag{8}$$

The time dependency is assumed to be $\exp(i\omega t)$, where ω is the circular frequency, and t is the time. Based on the time dependency, the governing equation and boundary condition for the wavefield are

$$\begin{aligned} L_{ij}(\partial)w_j(x) &= -N_{ij}(\partial, x)w_j(x) \\ n_j(x)T_{ijk}(\partial)w_k(x) &= \begin{cases} \tau_i(x) & x \in \Gamma_1 \subset B \\ 0 & x \in B \setminus \Gamma_1 \end{cases} \end{aligned} \tag{9}$$

where w_j is the displacement field (total wavefield), τ_i is the distributed load at Γ_1, and L_{ij}, N_{ij}, and T_{ijk} are the following differential operators:

$$L_{ij}(\partial) = (\lambda_0 + \mu_0)\partial_i\partial_j + \delta_{ij}\mu_0\partial_k\partial_k + \delta_{ij}\rho_0\omega^2 \tag{10}$$

$$\begin{aligned} N_{ij}(\partial, x) = &\left(\tilde{\lambda}(x) + \tilde{\mu}(x)\right)\partial_i\partial_j + \delta_{ij}\tilde{\mu}(x)\partial_k\partial_k + \left(\partial_i\tilde{\lambda}(x)\right)\partial_j \\ &+ \delta_{ij}(\partial_k\tilde{\mu}(x))\partial_k + \left(\partial_j\tilde{\mu}(x)\right)\partial_i + \delta_{ij}\tilde{\rho}(x)\omega^2 \end{aligned} \tag{11}$$

$$T_{ijk}(\partial, x) = \mu(x)\delta_{ik}\partial_j + \mu(x)\delta_{jk}\partial_i + \lambda(x)\delta_{ij}\partial_k \tag{12}$$

Note that δ_{ij} is the Kronecker delta, ∂_j is the partial differential operator, $n_j(x)$ is the normal vector of the boundary at the point x, and the subscript indicates the component of the coordinate system. The Green's function for the background structure of the wavefield is important in the formulation, as well as in the numerical calculations; this function is defined as

$$\begin{aligned} L_{ij}(\partial_x)G_{jk}(x, y) &= -\delta_{ik}\delta(x - y) \\ n_j(x)T^{(0)}_{ijk}(\partial_x)G_{kl}(x, y) &= 0, \quad (x \in B) \end{aligned} \tag{13}$$

where $x,\ y \in \mathbb{R}^3_+$ are the field and source points for the Green's function, ∂_x denotes the differential operator for the field point, $\delta(\cdot)$ is the Dirac delta function, and $G_{ij}(\cdot,\cdot)$ is the Green's function. Note that $T^{(0)}_{ijk}$ is the differential operator defined by

$$T^{(0)}_{ijk}(\partial) = \mu_0\delta_{ik}\partial_j + \mu_0\delta_{jk}\partial_i + \lambda_0\delta_{ij}\partial_k \tag{14}$$

We will use the spectral form of the Green's function (Touhei, 2009) for the numerical examples in this article; this is given by

$$G_{ij}(x,y) = \iint_{\mathbb{R}^2} \sum_{\xi\in\sigma_p} \frac{\Lambda_{ik}(\xi,x)\Lambda^*_{jk}(\xi,y)}{\mu_0\xi_3^2 - \rho_0\omega^2 + i\epsilon} \mathrm{d}\xi_1\mathrm{d}\xi_2 + \iint_{\mathbb{R}^2} \int_{\xi_r}^{\infty} \times \frac{\Lambda_{ik}(\xi,x)\Lambda^*_{jk}(\xi,y)}{\mu_0\xi_3^2 - \rho_0\omega^2 + i\epsilon} \mathrm{d}\xi\mathrm{d}\xi_1\mathrm{d}\xi_2 \tag{15}$$

where Λ_{ij} is an eigenfunction (Touhei, 2009), ξ is a point in the wavenumber space:

$$\xi = (\xi_1, \xi_2, \xi_3) \in \mathbb{R}^3_+ \tag{16}$$

and

$$\xi_r = \sqrt{\xi_1^2 + \xi_2^2} \tag{17}$$

In addition, σ_p in Eq. (15) is the subset in the wavenumber space $\mathbb{R}^3_+$ related to the Rayleigh wave mode that can be defined by

$$\sigma_p = \{\xi \in \mathbb{R}^3_+ \mid F(\xi) = 0\} \tag{18}$$

where $F(\xi)$ is the Rayleigh function (Aki and Richards, 2002) defined by

$$F(\xi) = \left(2\xi_r^2 - \xi_3^2\right)^2 - 4\xi^2\gamma\nu \tag{19}$$

$$\gamma = \sqrt{\xi_r^2 - (c_T/c_L)^2\xi_3^2}, \quad \nu = \sqrt{\xi_r^2 - \xi_3^2} \tag{20}$$

Note that c_T and c_L are, respectively, the velocities of the S and P waves in the background structure. Note that in the following discussion, we will use the subset of the wavenumber space $\mathbb{R}^3_+$ defined by

$$\sigma_c = \{\xi \in \mathbb{R}^3_+ \mid \xi_3 > \xi_r\} \tag{21}$$

2.2. Review of the basic results of the near-field equation

The following is the near-field equation that has a central role in the formulation of this article:

$$\int_{\Gamma_1} G^{(s)}_{ij}(x,y)\tau_j(y)\mathrm{d}\Gamma_1(y) = G_{ij}(x,z)\alpha_j, \quad (x \in \Gamma_2, \tau_j \in L_2(\Gamma_1)) \tag{22}$$

where $G^{(s)}_{ij}(x,y)$ is the scattered tensor describing the scattered wavefield as a function of x that is due to a unit point force applied to a point y, z is the probing point, and α_j is the force vector applied to the probing point. The near-field equation and its basic properties were introduced and proved by Fata and Guzina (2004) and Baganas et al. (2006). Their results, in part, are also used in this article and will be shown later in the form of Lemmas 1 and 2. The task of this section is a review of these basic results in accordance with the notation used in this article.

The incident wavefield due to the distributed load $\tau_j \in L_2(\Gamma_1)$ can be expressed as

$$u_i(x) = \int_{\Gamma_1} G_{ij}(x,y)\tau_j(y)\mathrm{d}\Gamma_1(y), \quad (x \in \mathbb{R}^3_+ \setminus \Gamma_1) \tag{23}$$

where u_i denotes the incident wavefield. By means of the scattered tensor, the scattered wavefield due to the distributed load τ_j can be expressed as

$$u^{(s)}_i(x) = \int_{\Gamma_1} G^{(s)}_{ij}(x,y)\tau_j(y)\mathrm{d}\Gamma_1(y), \quad (x \in \mathbb{R}^3_+) \tag{24}$$

It is also possible to interpret $u^{(s)}_i$ as the scattered wavefield due to the incident wave u_i (Baganas et al., 2006). The total wavefield is the sum of the incident wave and the scattered wave in the following form:

$$w_i(x) = u_i(x) + u^{(s)}_i(x) \tag{25}$$

which satisfies the Lippmann–Schwinger equation:

$$w_i(x) = u_i(x) + \int_E G_{ij}(x,y)N_{jk}(\partial,y)w_k(y)\mathrm{d}y, \quad (x \in \mathbb{R}^3_+) \tag{26}$$

For the interior of the fluctuated region E, the total wavefield can also be expressed in terms of Green's formula:

$$\begin{aligned} w_i(x) = u_i(x) &+ \int_E G_{ij}(x,y)N_{jk}(\partial,y)w_k(y)\mathrm{d}E(y) \\ &- \int_{\partial E} ((w_j(y) - u_j(y))P_{ij}(x,y) \\ &- \left(p_j(w,y) - p^{(0)}_j(u,y)\right)G_{ij}(x,y))\mathrm{d}s(y), \quad (x \in E^o) \end{aligned} \tag{27}$$

where

$$\begin{aligned} p^{(0)}_i(u,x) &= n_j(x)T^{(0)}_{ijk}(\partial)u_k(x) \\ p_i(w,x) &= \lim_{x\in E^o\to\partial E} n_j(x)T_{ijk}(\partial,x)w_k(x) \\ P_{ij}(x,y) &= n_k(y)T^{(0)}_{jkm}(\partial_y)G_{im}(x,y) \end{aligned} \tag{28}$$

For the derivation of Eq. (27), the representation of the incident wavefield inside E

$$u_i(x) = \int_{\partial E} \left(G_{ij}(x,y)p^{(0)}_j(u,y) - P_{ij}(x,y)u_j(y)\right)\mathrm{d}s(y), \quad x \in E^o \tag{29}$$

is used. It can be readily seen that Eq. (27) is equivalent to the following boundary value problem in E:

$$L_{ij}(\partial)u_j(x) = 0, \quad (x \in E^o) \tag{30}$$

$$L_{ij}(\partial)w_j(x) + N_{ij}(\partial,x)w_j(x) = 0, \quad (x \in E^o) \tag{31}$$

$$w_i(x) - u_i(x) = f_i(x), \quad (x \in \partial E) \tag{32}$$

$$p_i(w,x) - p^{(0)}_i(u,x) = h_i(x), \quad (x \in \partial E) \tag{33}$$

which is known as an *interior transmission problem*, where f_i and h_i are the trace of functions for the scattered wavefield:

$$\begin{aligned} f_i(x) &= u^{(s)}_i(x)|_{\partial E} \\ h_i(x) &= n_j(x)T^{(0)}_{ijk}(\partial)u^{(s)}_k(x)|_{\partial E} \end{aligned} \tag{34}$$

The following lemma is the characterization of the near-field equation in terms of the interior transmission problem, which was proved by Baganas et al. (2006).

Lemma 1. *Let $z \in E^o$ be fixed. The integral equation for the 1st kind (22) possesses the solution $\tau_j \in L_2(\Gamma_1)$ if and only if there exists a solution pair u_i and w_i given by*

$$L_{ij}(\partial_x)u_j(x) = 0, \quad (x \in E^o) \tag{35}$$

$$L_{ij}(\partial_x)w_j(x) + N_{ij}(\partial_x,x)w_j(x) = 0, \quad (x \in E^o) \tag{36}$$

$$w_i(x) - u_i(x) = G_{ij}(x,z)\alpha_j, \quad (x \in \partial E) \tag{37}$$

$$p_i(w,x) - p^{(0)}_i(u,x) = n_j(x)T^{(0)}_{ijk}(\partial_x)G_{kl}(x,z)\alpha_l, \quad (x \in \partial E) \tag{38}$$

where u_i is the incident wavefield expressed by Eq. (23).

Lemma 1 shows that Eq. (22) is solvable if and only if a pair of functions u_i and w_i solves the interior transmission problem of Eqs. (35)–(37). The problem that arises from this lemma is whether Eq. (23) can express the incident wave u_i for the pair of functions (u_i, w_i) that solves the interior transmission problem.

For this problem, Fata and Guzina (2004) proved that the set of incident wavefields spanned by $\tau_j \in L_2(\Gamma_1)$ in Eq. (23) is dense in a

space of the solutions of the homogeneous Navier equation in E with respect to the $H^1(E)$ norm:

$$\left\|u_i - S_{ij}\tau_j\right\|_{H^1(E)} < \epsilon' \tag{39}$$

where u_i is the solution of the homogeneous Navier equation in E and

$$\left(S_{ij}\tau_j\right)(x) = \int_{\Gamma_1} G_{ij}(x,y)\tau_j(y)\mathrm{d}\Gamma_1(y) \tag{40}$$

Application of the trace theorem to Eq. (39) leads to:

$$\|v_i\|_{H^{1/2}(\partial E)} < c_1\epsilon' \quad \left\|p_i^{(0)}(v,\cdot)\right\|_{H^{-1/2}(\partial E)} < c_1\epsilon' \tag{41}$$

where

$$v_i(x) = u_i(x) - \left(S_{ij}\tau_j\right)(x) \tag{42}$$

and c_1 is a positive constant. In addition, we can define a bounded linear operator $\mathcal{B}$ mapping from the boundary data of the homogeneous Navier equation in E to the scattered waves at the observation surface:

$$\mathcal{B} : H^{1/2}(\partial E) \times H^{-1/2}(\partial E) \ni \left(u_i, p_i^{(0)}(u,\cdot)\right) \longrightarrow u_i^{(s)} \in L_2(\Gamma_2) \tag{43}$$

Then, due to the boundness of the operator $\mathcal{B}$, we have the following for a positive constant $M > 0$:

$$\left\|\mathcal{B}\left(v_i, p_i^{(0)}(v,\cdot)\right)\right\|_{L_2(\Gamma_2)} \leqslant M\left[\|v_i\|^2_{H^{1/2}(\partial E)} + \left\|p_i^{(0)}(v,\cdot)\right\|^2_{H^{-1/2}(\partial E)}\right]^{1/2} \leqslant \sqrt{2}c_1 M\epsilon' \tag{44}$$

At this point, we should recall that for the near-field equation, the scattered wavefield is represented by

$$u_i^{(s)}(x) = G_{ij}(x,z)\alpha_j, \quad (x \in E^c, z \in E^o) \tag{45}$$

as a result of the incident wavefield u_i. Therefore, we have the following:

$$\mathcal{B}\left(v_i, p_i^{(0)}(v,\cdot)\right) = G_{ij}(x,z)\alpha_j - \int_{\Gamma_1} G_{ij}^{(s)}(x,y)\tau_j(y)\mathrm{d}\Gamma_1(y), \quad (x \in \Gamma_2) \tag{46}$$

From this, Baganas et al. (2006) showed the following:

Lemma 2. *Let $z \in E^o$ be fixed. Then, $\forall\epsilon > 0$, there exists $\tau_j(\cdot,\epsilon) \in L_2(\Gamma_1)$ such that*

$$\left\|\int_{\Gamma_1} G_{ij}^{(s)}(\cdot,y)\tau_j(y,\epsilon)\mathrm{d}\Gamma_1(y) - G_{ij}(\cdot,z)\alpha_j\right\|_{L_2(\Gamma_2)} < \epsilon \tag{47}$$

For simplicity, in the following, we will express the near-field equation as follows:

$$\left(F_{ij}\tau_j\right)(x) = G_{ij}(x,z)\alpha_j \tag{48}$$

where F is the near-field operator defined by

$$\left(F_{ij}\tau_j\right)(x) := \int_{\Gamma_1} G_{ij}^{(s)}(x,y)\tau_j(y)\mathrm{d}\Gamma_1(y), \quad \left(x \in \Gamma_2, \tau_j \in L_2(\Gamma_1)\right) \tag{49}$$

Eqs. (26) and (48) and Lemma 2 constitute the basis of the following formulation. Unlike the standard linear sampling method, we will not use the divergence properties of the solution of the near-field equation.

2.3. Definition of the solvability index for the near-field equation

In this article, instead of solving Eq. (48), we introduce the following characteristic function:

$$\phi(z) = \inf_{\tau_j \in L_2(\Gamma_1)} \left\|G_{ij}(\cdot,z)\alpha_j - \left(F_{ij}\tau_j\right)(\cdot)\right\|_{L_2(\Gamma_2)} \tag{50}$$

Roughly speaking, the mathematical meaning of the function is

$$\begin{cases} \phi(z) = 0 & \text{when Eq. (48) is solvable} \\ \phi(z) > 0 & \text{when Eq. (48) is not solvable} \end{cases} \tag{51}$$

and as a result of the above properties, we will call $\phi(z)$ the *solvability index*. In this section, we will investigate the properties of the solvability index by considering an application of a factorization of the operator (Kirsch, 2011).

First, let us express the kernel of the near-field operator by using the Lippmann–Schwinger equation:

$$G_{ij}^{(s)}(x,y) = \int_E G_{ik}(x,z)N_{kl}(\partial_z,z)G_{lj}(z,y)\mathrm{d}E(z) + \int_E G_{ik}(x,z)N_{kl}(\partial_z,z)G_{lj}^{(s)}(z,y)\mathrm{d}E(z), \quad (x \in \Gamma_2, y \in \Gamma_1) \tag{52}$$

According to Eq. (52), when the Born approximation is valid for the wavefield, the kernel of the near-field operator can be simplified to

$$G_{ij}^{(s)}(x,y) = \int_E G_{ik}(x,z)N_{kl}(\partial_z,z)G_{lj}(z,y)\mathrm{d}E(y), \quad (x \in \Gamma_2, y \in \Gamma_1) \tag{53}$$

which leads directly to the factorization of the near-field operator in the following form:

$$F_{ij} = W_{ik}\mathcal{N}_{kl}U_{lj} \tag{54}$$

where

$$\left(U_{lj}f_j\right)(z) = \int_{\Gamma_1} G_{lj}(z,y)f_j(y)\mathrm{d}\Gamma_1(y), \quad \left(z \in E, f_j \in L_2(\Gamma_1)\right) \tag{55}$$

$$\left(\mathcal{N}_{kl}\varphi_l\right)(z) = N_{kl}(\partial_z,z)\varphi_l(z), \quad (z \in E, \varphi \in C^\infty(E)) \tag{56}$$

$$\left(W_{ik}g_k\right)(x) = \int_E G_{ik}(x,z)g_k(z)\mathrm{d}E(z), \quad \left(x \in \Gamma_2, g_j \in L_2(E)\right) \tag{57}$$

Even when the Born approximation is not valid, the factorization of the near-field operator is possible. Due to the Lippmann–Schwinger equation, the scattered wavefield can be expressed as

$$u_i^{(s)}(x) = \int_E G_{ij}(x,z)N_{jk}(\partial_z,z)\left(u_k^{(s)}(z) + u_k(z)\right)\mathrm{d}E(z) \tag{58}$$

Therefore, let us define an operator $\mathcal{M}_{jk}$ as follows:

$$\left(\mathcal{M}_{jk}u_k\right)(z) := N_{jk}(\partial_z,z)\left(u_k^{(s)}(z) + u_k(z)\right), \quad u_k^s, u_k \in C^\infty(E) \tag{59}$$

Then, the near-field operator can be decomposed as

$$F_{ij} = W_{ik}\mathcal{M}_{kl}U_{lj} \tag{60}$$

Next, we investigate the following integral equation:

$$\int_E G_{ij}(x,y)g_j(y)\mathrm{d}E(y) = G_{ij}(x,z)\alpha_j, \quad (g_j \in L_2(E), x \in E^c) \tag{61}$$

When $z \in E^c$, it is clear that we cannot find a solution g_j to Eq. (61), since the right-hand side of the equation is unbounded, while the left-side of the equation is bounded. Even for this case, let us assume that

$$\left\|G_{ij}(\cdot,z)\alpha_j - \int_E G_{ij}(\cdot,y)g_j(y)\mathrm{d}E(y)\right\|_{L_2(\Gamma_2)} = 0, \quad (z \in E^c) \tag{62}$$

can be established.

Then, based on the discussion by Fata and Guzina (2004) for the use of Holmgren's uniqueness theorem (Colton, 1980), the following equation holds:

$$\int_E G_{ij}(x,y)g_j(y)\mathrm{d}E(y) = G_{ij}(x,z)\alpha_j, \quad (z \in E^c, x \in E^c \setminus V_\delta(z)) \tag{63}$$

where $V_\delta(z)$ is the neighborhood of z such that

$$V_\delta(z) = \{x \in \mathbb{R}^3_+ \mid |x - z| < \delta\} \tag{64}$$

It is clear that Eq. (63) has no solutions. As a result, we obtain

$$\forall g_j \in L_2(E),\ \left\| G_{ij}(\cdot, z)\alpha_j - \int_E G_{ij}(\cdot, y) g_j(y) \mathrm{d}E(y) \right\|_{L_2(\Gamma_2)} > 0, \quad (z \in E^c) \tag{65}$$

which shows

$$G_{ij}(\cdot, z)\alpha_j \notin \operatorname{ran} W \ (z \in E^c) \tag{66}$$

where ran W denotes the range of the operator W. We can see that

$$\operatorname{ran} F \subset \operatorname{ran} W \tag{67}$$

Therefore,

$$\forall \tau_j \in L_2(\Gamma_1),\ \left\| G_{ij}(\cdot, z)\alpha_j - (F_{ij}\tau_j)(\cdot)(y) \right\|_{L_2(\Gamma_2)} > 0, \quad (z \in E^c) \tag{68}$$

and as a result

$$\phi(z) = \inf_{\tau_j \in L_2(\Gamma_1)} \left\| G_{ij}(\cdot, z)\alpha_j - (F_{ij}(\tau_j))(\cdot) \right\|_{L_2(\Gamma_2)} > 0, \quad (z \in E^c) \tag{69}$$

Based on Lemma 2 and Eq. (69), we have the following theorem:

Theorem 1. *The solvability index has the following properties:*

$$\phi(z) = 0, \quad (z \in E^o) \tag{70}$$

$$\phi(z) > 0, \quad (z \in E^c) \tag{71}$$

The concept of the physical meaning of the solvability index is shown in Fig. 2. The scattered waves are from the fluctuations. Theorem 1 shows that Green's function from the probing point inside the fluctuation can be well approximated by the scattered waves due to the distributed load at Γ_2. As a result, we have $\phi(z) = 0$. On the other hand, when the probing point is outside the region of a fluctuating wavefield, the paths of the Green's function and the scattered waves will be different. Therefore, the approximation is not possible, and as a result, $\phi(z) > 0$.

2.4. Singular value decomposition of the near-field operator for evaluating the solvability index

In general, evaluation of the infimum of a functional is not an easy task. For the solvability index defined by Eq. (50), however, we can use a simplified evaluation method. The purpose of this section is to formulate this evaluation method. According to the literature (for example, Akhiezer and Glazman, 1981), it can be readily seen from Eq. (50) that $\phi(z)$ denotes the distance between the function $G_{ij}(x, z)\alpha_j$ and the range of the operator F, which is a subspace of the Hilbert space $L_2(\Gamma_2)$. The orthogonal decomposition of $L_2(\Gamma_2)$ is also possible by means of the operator F:

$$L_2(\Gamma_2) = \overline{\operatorname{ran}}\, F \oplus \ker F^*, \quad \left((\ker F^*)^\perp = \overline{\operatorname{ran}}\, F \right) \tag{72}$$

where F^* is the adjoint operator for F and satisfies

$$\left(\psi_i, F_{ij}\varphi_j \right)_{L_2(\Gamma_2)} = \left(F^*_{ij}\psi_i, \varphi_j \right)_{L_2(\Gamma_1)}, \quad (\psi_i \in L_2(\Gamma_2),\ \varphi_i \in L_2(\Gamma_1)) \tag{73}$$

$\ker F^*$ is defined by

$$\ker F^* = \{\psi_i \in L_2(\Gamma_2) \mid F^*_{ij}\psi_j = 0\} \tag{74}$$

and $\overline{\operatorname{ran}}\, F$ is the closure of the range of the operator F.

Now, let us define the projection

$$\mathcal{P} : L_2(\Gamma_2) \longrightarrow \overline{\operatorname{ran}}\, F \tag{75}$$

according to the orthogonal decomposition shown in Eq. (72). Then, based on the projection theorem for a Hilbert space (Akhiezer and Glazman, 1981), we can evaluate the solvability index as follows:

$$\phi(z) = \left\| G_{ij}(\cdot, z)\alpha_j - \left(\mathcal{P}_{ij} G_{jk}(\cdot . z)\alpha_k \right)(x) \right\|_{L_2(\Gamma_2)} \tag{76}$$

Therefore, the task of evaluating the infimum of the norm has been replaced by the task of constructing this projection. The geometrical aspects of the evaluation of the solvability index are shown in Fig. 3.

Construction of the projection in this way is possible due to the singular value decomposition of the operator. As in the literature (Colton and Kress, 1998), let us define the singular value problem as follows:

$$F_{ij}\varphi^{(n)}_j = \theta_n \psi^{(n)}_i, \quad F^*_{ik}\psi^{(n)}_i = \theta_n \varphi^{(n)}_k, \quad (n = 1, 2, \ldots) \tag{77}$$

where $(\theta_n, \varphi^{(n)}_i, \psi^{(n)}_i), n \in \mathbb{N}$ is the singular system of the operator F. Note that the singular value problem defined by Eq. (77) can also be written as

$$F^*_{ik}F_{ij}\varphi^{(n)}_j = \theta^2_n \varphi^{(n)}_k \tag{78}$$

$$\psi^{(n)}_i = \frac{1}{\theta_n} F_{ij}\varphi^{(n)}_j, \quad (n = 1, 2, \ldots) \tag{79}$$

from which the orthogonality relationship of the singular value system is derived. Since the set of the singular values are the nonzero values of θ_n, the orthogonality relationship of the singular system can be expressed as

$$\begin{aligned} \left(\varphi^{(n)}_i, \varphi^{(m)}_i \right)_{L_2(\Gamma_1)} &= \delta_{nm} \\ \left(\psi^{(n)}_i, \psi^{(m)}_i \right)_{L_2(\Gamma_2)} &= \delta_{nm} \end{aligned} \tag{80}$$

It has been shown (Colton and Kress, 1998) that

$$f_i = \sum_{n=1}^{\infty} \left(\psi^{(n)}_j, f_j \right)_{L_2(\Gamma_2)} \psi^{(n)}_i, \quad \forall f_i \in \overline{\operatorname{ran}}\, F \tag{81}$$

when

$$\sum_{n=1}^{\infty} \frac{1}{\theta^2_n} |(\psi^{(n)}_j, f_j)|^2 < \infty \tag{82}$$

According to Eq. (81), $\{\psi^{(n)}_i\}_{n=1}^{\infty}$ is an orthonormal basis that spans the range of the closure of the operator F. Therefore, the representation of the projection defined by Eq. (75) becomes

$$\left(\mathcal{P}_{ij} f_j \right)(x) = \sum_{n=1}^{\infty} \left(\psi^{(n)}_j, f_j \right)_{L_2(\Gamma_2)} \psi^{(n)}_i(x), \quad (\forall f_j \in L_2(\Gamma_2)) \tag{83}$$

At this point, we must consider a treatment for an ill-posed problem. It is known that an ill-posed problem will be confronted when solving the 1st kind of Fredholm equation, such as the near-field equation. In such a case, a regularization scheme is required. When the singular values for the operator are known, it is possible to use the spectral cutoff as the regularization scheme (Colton and Kress, 1998). According to the Picard theorem (Colton and Kress, 1998), the solution of Eq. (48) is expressed by

$$\tau_i = \sum_{n=1}^{\infty} \frac{1}{\theta_n} \left(\psi^{(n)}_j, f_j \right) \varphi^{(n)}_i \tag{84}$$

when $f_i \in \overline{\operatorname{ran}}\, F$ and Eq. (82) is fulfilled. According to the literature (Colton and Kress, 1998), when the spectral cutoff is applied as the regularization scheme, the solution to Eq. (48) is

$$\tau_i = \sum_{\theta_n > \theta_m} \frac{1}{\theta_n} \left(\psi^{(n)}_j, f_j \right) \varphi^{(n)}_i \tag{85}$$

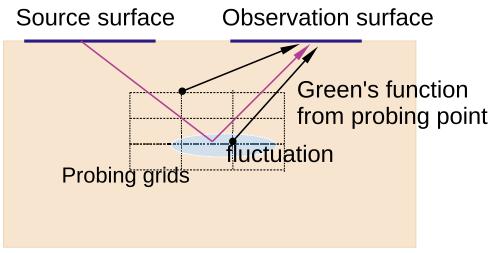

Fig. 2. Paths of scattered waves and Green's functions from the probing points.

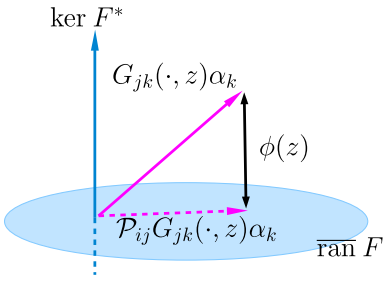

Fig. 3. Conceptual view of the solvability index.

Note that this expression of the solution to Eq. (85) neglects the contribution from the eigenfunctions for which the singular values are less than θ_m. As in Eq. (85), the expression of the projection for which the spectral cutoff has been applied is

$$(\mathcal{P}_{ij}f_j)(x) = \sum_{\theta_n>\theta_m} \left(\psi_j^{(n)}, f_j\right)_{L_2(\Gamma_2)} \psi_i^{(n)}(x), \quad (\forall f_j \in L_2(\Gamma_2)) \tag{86}$$

We are now able to solve Eq. (76) by using the singular value decomposition of the projection. In the next section, the necessity of the regularization scheme will also be discussed.

In addition, we must take into account the fact that the amplitude of the Green's function strongly depends on the depth of the point source. Therefore, the excitation force at the probing point is adjusted as follows:

$$\|G_{ij}(x,z)\alpha_j\|_{L_2(\Gamma_2)} = 1 \tag{87}$$

3. Numerical examples

3.1. Inversion of two box-shaped inclusions

3.1.1. Analysis of model

In the first numerical example, we will reconstruct the location and spatial spread of the fluctuations due to two box-shaped inclusions, as shown in Fig. 4. The two box-shaped fluctuations are both embedded at a depth of 5 km, and they are in the form of cubes with a side length of 3 km. For the background structure of the wavefield, the velocities of the S and P waves are set at 1 km/s and 2 km/s, respectively, and the mass density is 2 g/cm^3. The fluctuations are defined as follows:

$$\begin{aligned} \tilde{\lambda}(x) &= 0.1\chi_Q(x) \text{ GPa}, \\ \tilde{\mu}(x) &= 0.1\chi_Q(x) \text{ GPa}, \\ \tilde{\rho}(x) &= 0 \text{ g/cm}^3 \end{aligned} \tag{88}$$

where χ_Q is the characteristic function defined as

$$\chi_Q(x) = \begin{cases} 1 & x \in Q \\ 0 & x \notin Q \end{cases} \tag{89}$$

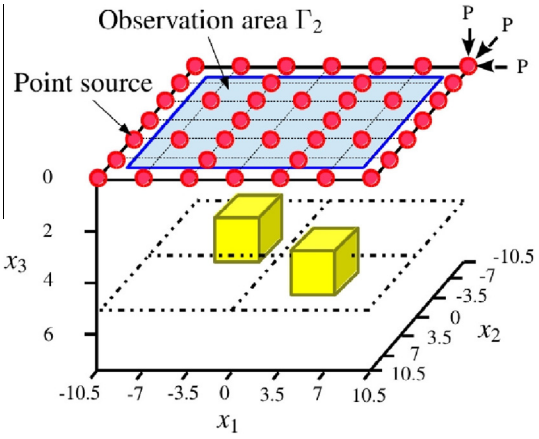

Fig. 4. Target model with two box-shaped fluctuations.

and Q is the each of the boxed regions. Note that the function for the fluctuations is in the class C_0^1, as was shown in the theoretical formulation. When performing numerical calculations, however, this restriction is relaxed due to the introduction of a discretized grid. The kernel of the near-field operator used in this section is based on the Born approximation. The wavefields are calculated using a fast method for solving the volume integral equation (Touhei, 2011).

As can be seen in Fig. 4, the source and observation surfaces are both set just above the region of the fluctuations. The excitation frequency of the source is 1 Hz. We performed numerical calculations to examine the effect on the accuracy of the reconstruction results when there was an increase in the grid density of the source, which is related to an increase in the range of the scattered tensor. We considered four cases (case s1 to case s4), each with a different model for a surface source; the definitions of the cases, including the location and number of the source points, are summarized in Table 1 and Fig. 5(a)–(d). For the observation surface, the location of the observation grids is shown in Fig. 6; the grid contains one hundred points. A triaxial point source was applied at each grid point of the source, and the three components of the scattered waves are observed at each grid point on the observation surface. In order to take into account the effects of the triaxial point force, we modified the solvability index defined by Eq. (76) as follows:

$$\phi(z) = \sqrt{\sum_{l=1}^{3} \left\| G_{ij}(\cdot,z)\alpha\delta_{jl} - \left(\alpha\mathcal{P}_{ij}G_{jk}(\cdot,z)\delta_{kl}\right)(x) \right\|_{L_2(\Gamma_2)}^2} \tag{90}$$

3.1.2. Results of the singular value decomposition

Fig. 7(a)–(d) show the distribution of the singular values for the scattered tensor for cases s1 to s4, respectively. In each case, the largest singular values were approximately 1.0×10^{-3}. On the other hand, when the number of point sources increased, the lowest singular value approached zero. The increase in the number of point sources reflects the fact that the scattered tensor itself is a

Table 1
Case studies for the source surface.

Case	Grid points	Reference
Case s1	9	Fig. 5(a)
Case s2	36	Fig. 5(b)
Case s3	49	Fig. 5(c)
Case s4	64	Fig. 5(d)

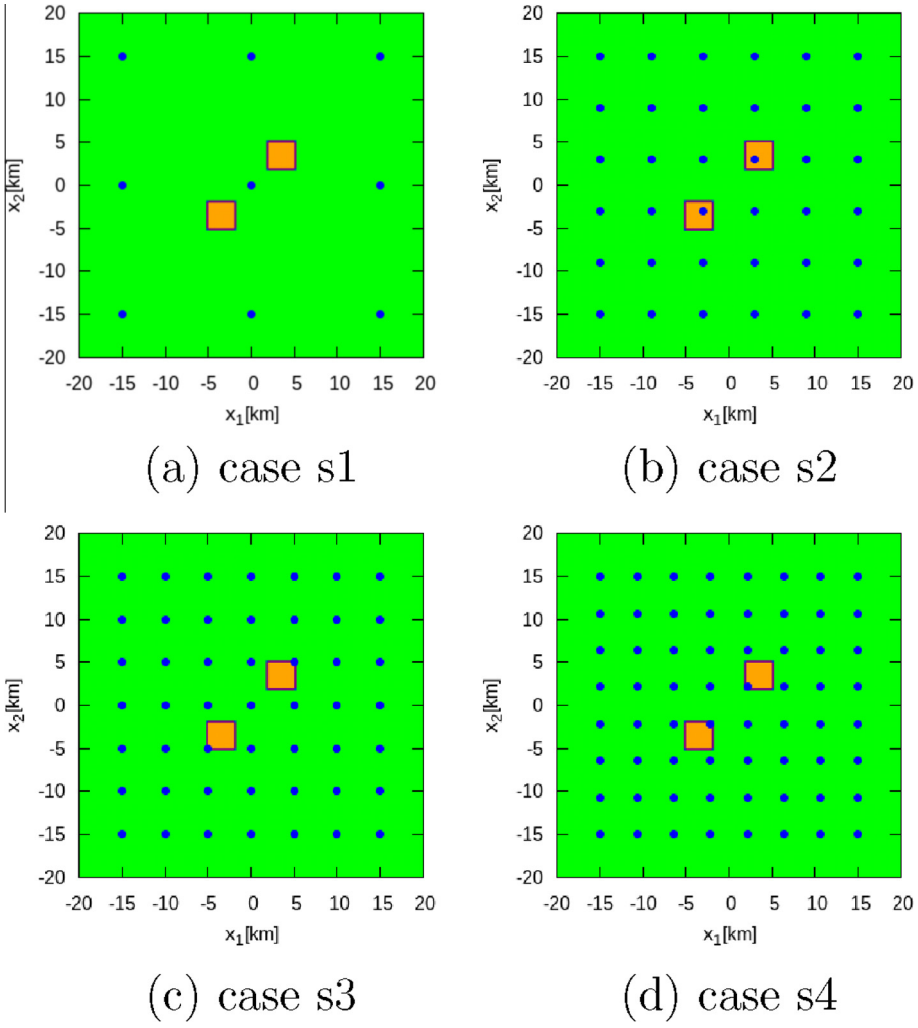

Fig. 5. Locations and numbers of point sources at the source surface.

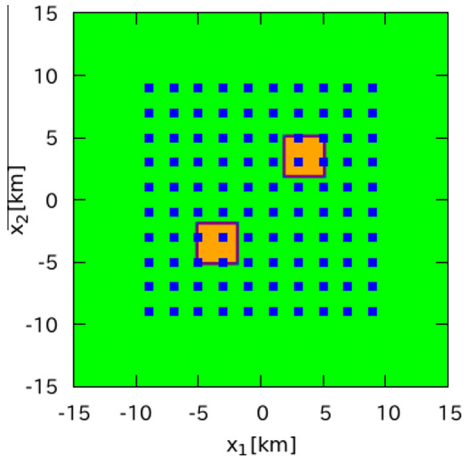

Fig. 6. Location of the observation grid points at the observation surface.

compact operator, and so its singular values converge to zero. As mentioned above, the spectral cutoff method is a way to regularize an ill-posed problem, such as this inverse scattering analysis. In the following numerical examples, however, all of the singular values obtained from the analysis were included when constructing the projection $\mathcal{P}_{ij}$, which is the map from $L_2(\Gamma_2)$ to $\overline{\mathrm{ran}}\, F$.

3.1.3. Results of reconstructing the fluctuations

Fig. 8(a)–(d) show the horizontal spatial distribution at a depth of 5 km for the solvability index for cases s1 to s4, respectively. The spatial spreads of each of the solvability indices were normalized so that the maximum amplitude was equal to unity. In the figures, the boxed areas (green lines) indicate the fluctuations of the target model. It can be clearly seen from Fig. 8(a)–(d) that the areas in which the solvability index has a low amplitude are strongly correlated with the fluctuations. The effects of an increase in the surface point sources can also be recognized in the reconstruction of the fluctuations. This means that it is not very easy to distinguish fluctuations from ghosts in case s1, but it is easy to do so in case s4. Furthermore, Fig. 8(d), which shows case s4, clearly shows that the low-amplitude areas of the solvability index are in good agreement with the spatial spread of the fluctuations of the target model.

Fig. 9(a)–(d) show the spatial spread of the solvability indices in the vertical plane at $x_2 = 3$ km; we used this to investigate the accuracy of the reconstructions in the vertical direction. In Fig. 9(a)–(d), the border of the target area is indicated by green lines. The improvement in accuracy due to an increase in the number of point sources can be seen here, as well as in Fig. 8(a)–(d).

As mentioned above, the spectral cutoff method was not used to regularize these numerical examples. In spite of this, we were able to accurately reconstruct the fluctuations due to an increase in the point sources.

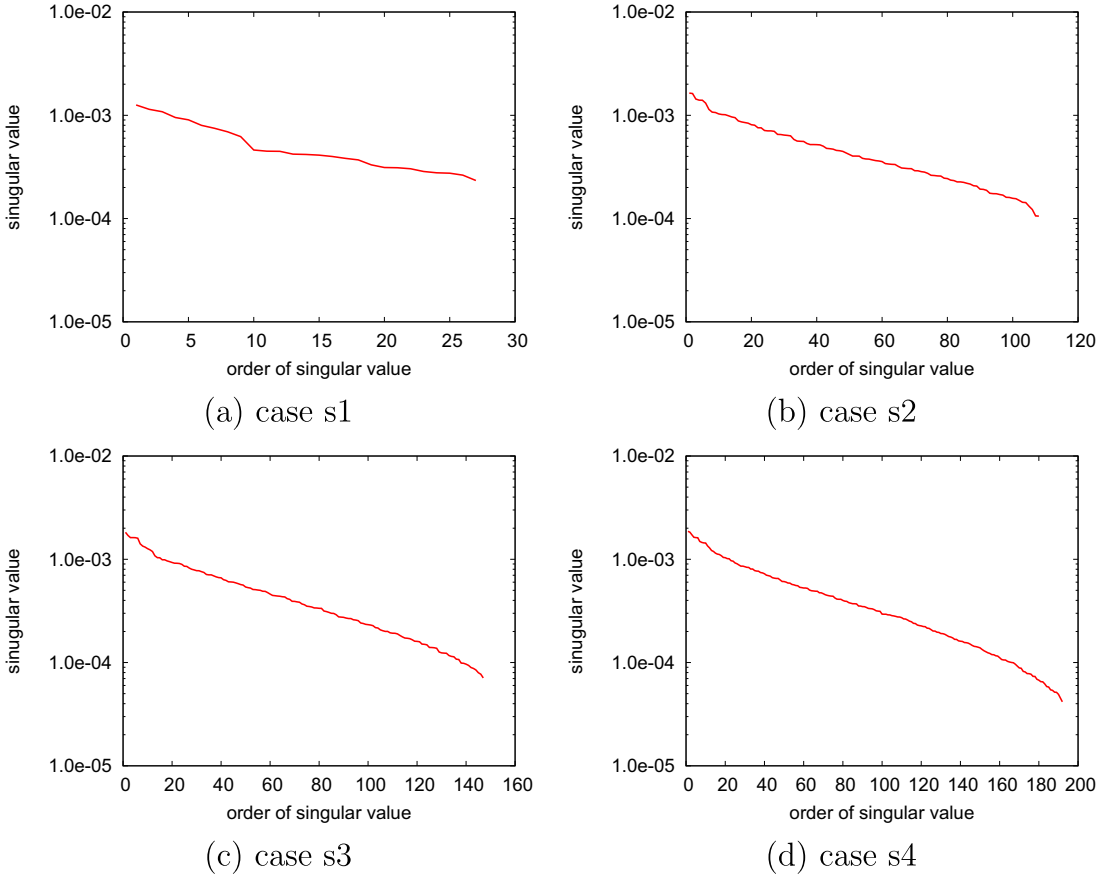

Fig. 7. Properties of the singular values for cases s1–s4.

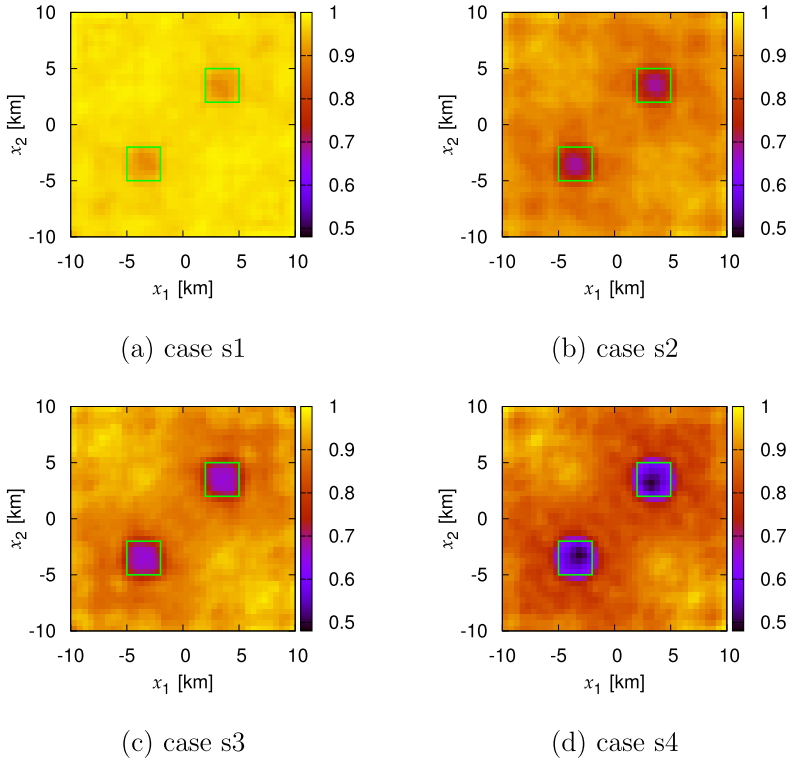

Fig. 8. Reconstruction of the fluctuations in the horizontal plane at a depth of 5 km.

3.1.4. Effects of random noise in the scattered waves when reconstructing the fluctuations

In the previous numerical examples, the effects of random noise were not included in the analysis of the observed scattered waves, but we will do this here. Fig. 10 shows the effects of random noise on the reconstructed results in a horizontal plane at a depth of $x_3 = 5$ km for case s4. The level of noise is defined as the ratio of the L_2 norms of the noise and the scattered waves, which are 10% and 20%, respectively. Fig. 11 also shows the effects of random noise at the vertical plane of $x_2 = 3$ km for case s4. We did not employ a regularization scheme when investigation these effects. According to Figs. 10 and 11, the presence of the random noise reduces the contrast of the amplitude and the area in which the solvability index has a low amplitude. Even in this situation, when the random noise is at the 20% level, it is almost possible to estimate the fluctuation.

3.1.5. Distribution of the norm of the solution to the near-field equation

The standard linear sampling method examines the spatial distribution of the norm of the solution to the inversion equation. Therefore, for the present problem, it is also important to examine the spatial distribution of the norm of the solution to the near-field equation in order to compare it with the spatial distribution of the solvability index. Fig. 12 shows the distribution of the norm of the solution for case s4. The solution of the near-field equation shown there is the result due to Eq. (84), in which the spectral cutoff was not applied; this was done to allow for comparison with the spatial distribution of the solvability index. In addition, the effects of the random noise were not considered. According to Fig. 12, the areas in which the norm of the solution has a lower amplitude correspond to the areas in which there are fluctuations. The standard linear sampling method uses the divergence of the solution of the inversion equation outside the scattering objects. Therefore, the tendency of the spatial distribution of the norm of the solution shown in Fig. 12 agrees with the properties of the linear sampling method. However, in the results, there are many ghosts around the target. One of the reasons for this may be that we did not use a regularization scheme; further investigation is necessary. At present, it can be said that the method based on the solvability index is free from these ghosts, even when regularization is not employed.

3.2. Reconstruction of scattered box-shaped fluctuations

3.2.1. Analysis of the model

In the next example, we reconstruct the fluctuations of a more complex target model. Here, the target model consists of several cube-shaped inclusions; the sides of the cube are each equal to 1 km. An overhead view of the fluctuation model is shown in Fig. 13. The cubes were placed at depths of from 2 km to 7 km and within a horizontal range of 5 km^2. The background structure of the wavefield and the amplitude of the fluctuations were the same as in the previous numerical examples. The source and observation surfaces were set above the fluctuations, as shown in Fig. 14. The observation grid was 13×13, and the source grid was 7×7. The source grid was distributed such that the incident waves could be observed over a wider area, and the observation grid was made more dense in order to gather information about the scattered waves in a narrower area. A triaxial force excitation was also employed here, and the excitation frequency was 1 Hz.

3.2.2. Reconstruction of the fluctuations at the horizontal planes

Prior to showing the results of the reconstructed fluctuations, we will discuss Fig. 15, which shows the results of the singular value analysis. The singular values are in the range from 2.0×10^{-3} to 2.0×10^{-5}, which is almost the same as in the previous analysis. Again, we did not apply a spectral cutoff. Note that all of the singular values were used to construct the projection in order to evaluate the solvability index.

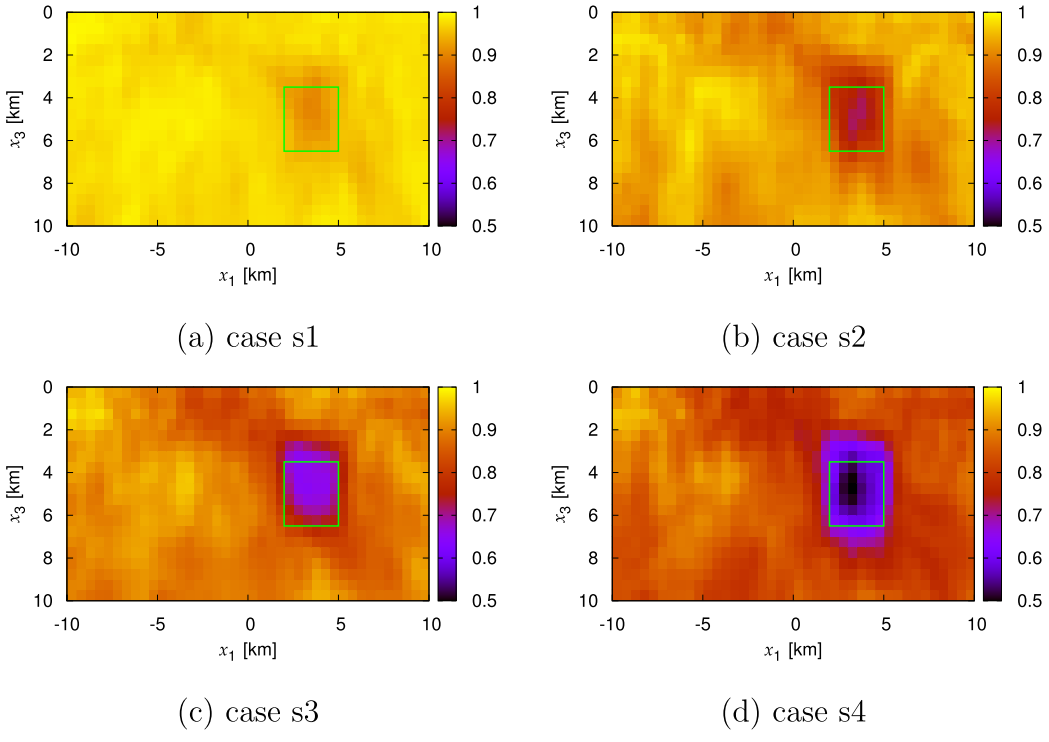

Fig. 9. Reconstruction of the fluctuations in the vertical plane at $x_2 = 3$ km.

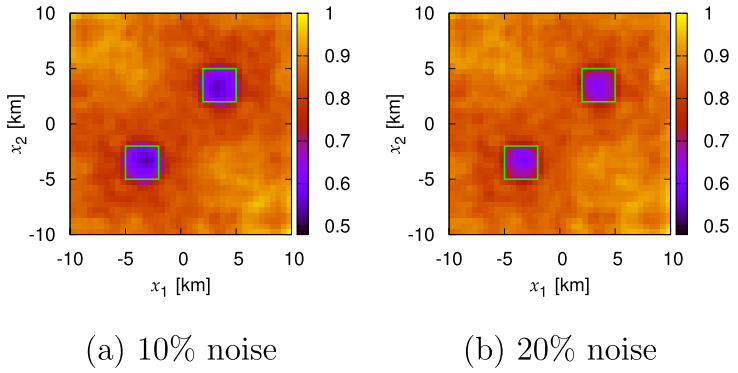

Fig. 10. Effects of random noise on the reconstruction of the fluctuation at a depth of $x_3 = 5$ km.

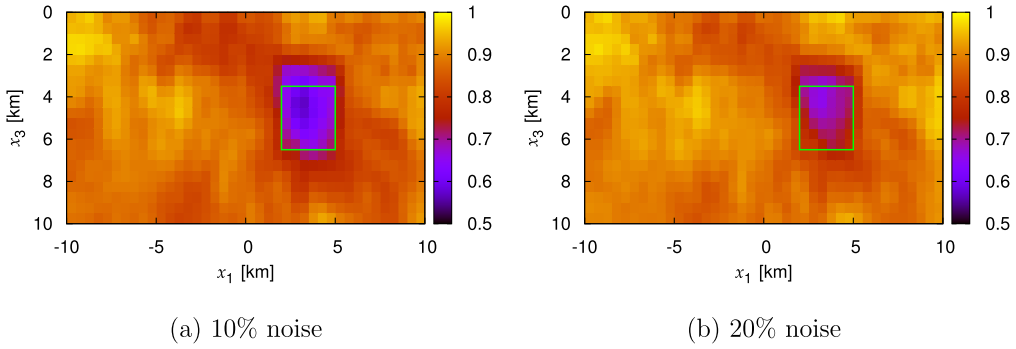

Fig. 11. Effects of random noise on the reconstruction of the fluctuation at a depth of $x_2 = 3$ km.

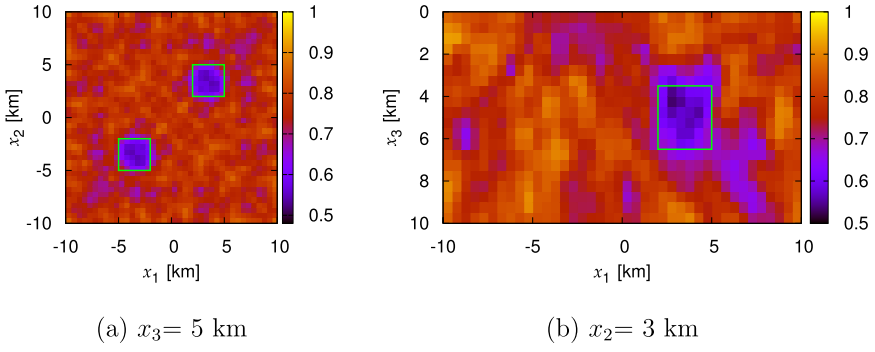

Fig. 12. Distribution of the norm of the solution of the near-field equation.

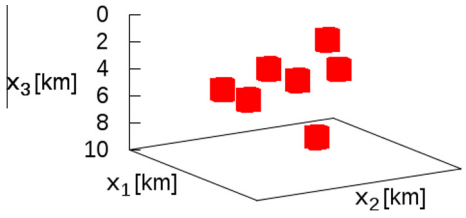

Fig. 13. Overhead view of the locations of the box-shaped fluctuations.

The reconstructed fluctuations at the horizontal planes are shown in Fig. 16(a)–(d); the depths of the horizontal planes are from 2 km to 7 km. For each result, the border of the fluctuations is indicated by solid green lines. It can be seen in Fig. 16(a)–(c) that the reconstructed fluctuations are in agreement with the target model at depths of from 2 km to 5 km. On the other hand, we see in Fig. 16(d) that at a depth of 7 km, it is difficult to distinguish the fluctuations from the ghosts. Therefore, at greater depths, it becomes difficult to distinguish between ghosts and targets. This may be due to the amount of information in the scattered tensor about the scattered waves from the deep regions. To improve the accuracy of the reconstruction in deep regions, the source and

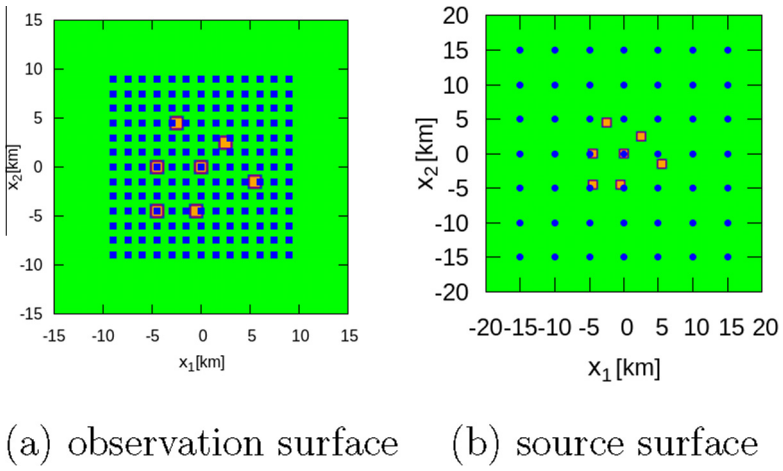

Fig. 14. Observation and source grids on the relevant surfaces.

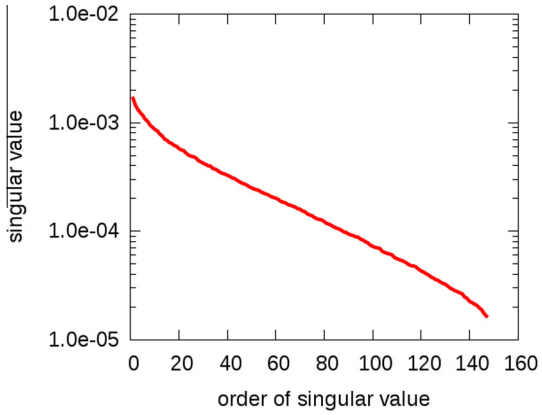

Fig. 15. Singular value decomposition.

observation surfaces will require readjustments to catch more information about the fluctuations in deep regions; this is left as a future task.

3.2.3. Reconstruction of the fluctuations at the vertical planes

Fig. 17(a)–(d) show the results of the reconstruction of the fluctuations in the vertical planes. All of the results shown in Fig. 17(a)–(d) indicate that the targets and the areas in which the solvability index has a low amplitude are in good agreement. Furthermore, in general, those areas that are taller than the target become clearer as the target nears the free surface. Therefore, as can be seen in Fig. 17(b), which shows the reconstruction of a deep part of the wavefield, the low-amplitude area of the solvability index is not very clear around the target, and its amplitude is comparable with that of the ghosts; this leads to the difficulty discussed above regarding Fig. 16(d).

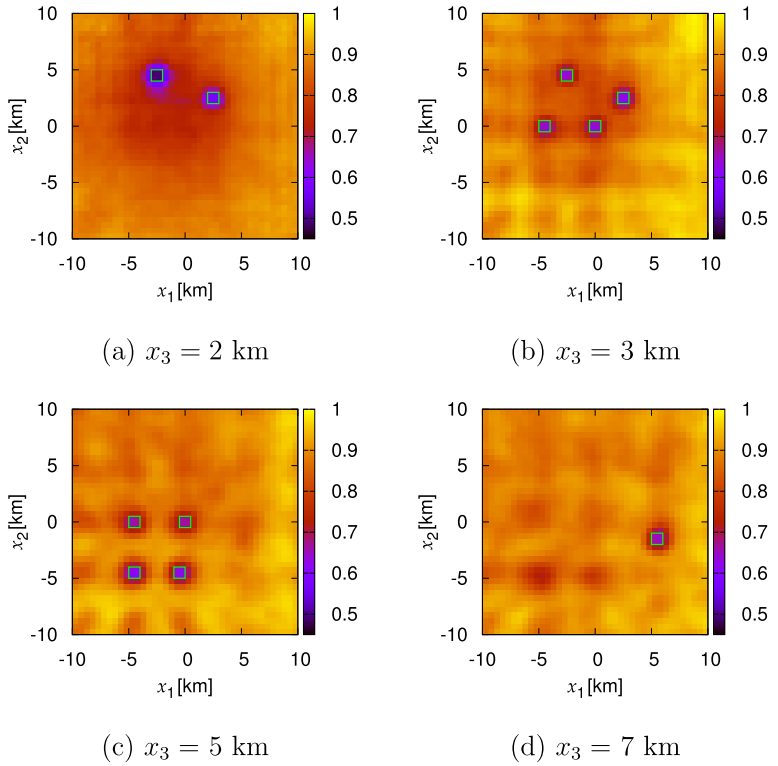

Fig. 16. Reconstruction of the fluctuations at the horizontal planes.

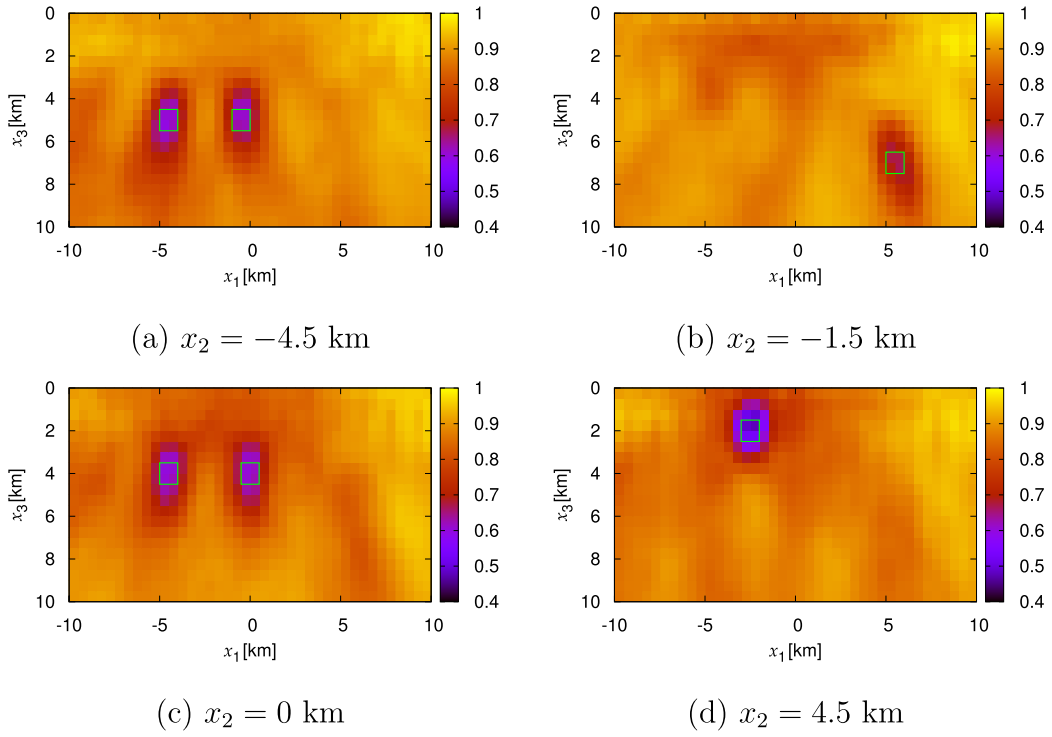

Fig. 17. Reconstruction of the fluctuations at the vertical planes.

4. Conclusions

In this study, we have developed a linear sampling method for reconstructing the fluctuations in an elastic half-space. In order to detect the fluctuations, we developed a solvability index for the near-field equation. According to the formulation, the amplitude of the solvability index corresponds to the spatial spread and location of the fluctuations of the wavefield. We also performed a comprehensive evaluation of the solvability index, which is based on a projection theorem for a Hilbert space and the singular value decomposition of the scattered tensor. Several numerical experiments revealed that an increase in the number of grid points for the source improves the accuracy of the reconstructions. In addition, the proposed method was also found to be applicable to a rather complex model of the fluctuations. In the numerical calculations, it was not necessary to use a spectral cutoff in order to obtain the reconstructed fluctuations.

References

Akhiezer, N.I., Glazman, I.M., 1981. Theory of Linear Operators in Hilbert Space, vol. 1. Pitman Advanced Publishing Program, London.
Aki, K., Richards, P.G., 2002. Quantitative Seismology, second ed. University Science Books, California.
Baganas, K., Guzina, B.B., Charalambopoulos, A., Manolis, G.D., 2006. A linear sampling method for the inverse transmission problem in near-field elastodynamics. Inv. Probl. 22, 1835–1853.
Campman, X., Herman, G., Muyzert, E., 2006. Suppressing near-receiver scattered waves from seismic land data. Geophysics 71 (4), S121–S128.
Colton, D., 1980. Analytic Theory of Partial Differential Equations. Pitman, London.
Colton, D., Kirsch, A., 1996. A simple method for solving inverse scattering problems in the resonance region. Inv. Probl. 12, 383–393.
Colton, D., Kress, R., 1998. Inverse Acoustic and Electromagnetic Scattering Theory. Springer, Berlin.
Fata, S.N., Guzina, B.B., 2004. A linear sampling method for near-field inverse problems in elastodynamics. Inv. Probl. 20, 713–736.
Gélis, C., Virieux, J., Grandjean, G., 2007. 2D elastic waveform inversion using Born and Rytov approximation in the frequency domain. Geophys. J. Int. 168, 605–633.
Guzina, B.B., Madyarov, A.I., 2007. A linear sampling approach to inverse elastic scattering in piecewise-homogeneous domains. Inv. Probl. 23, 1467–1493.
Guzina, B.B., Fata, S.N., Bonnet, M., 2003. On the stress-wave imaging of cavities in a semi-infinite solid. Int. J. Solids Struct. 40, 1505–1523.
Kirsch, A., 2011. The factorization method for inverse problems. Newton Institute. <http://www.newton.ac.uk/files/seminar/20110728090009451-152765.pdf>.
Pelekanos, G., Abubakar, A., van den Berg, P.M., 2004. Contrast source inversion methods in elastodynamics. J. Acous. Soc. Am. 114, 2825–2834.
Romdhane, A., Grandjean, G., Brossier, R., Réjiba, F., Operto, S., Virieux, J., 2011. Shallow structures characterization by 2D elastic waveform inversion. Geophysics 76 (3), R81–R93.
Touhei, T., 2009. Generalized Fourier transform and its application to the volume integral equation for elastic wave propagation in a half space. Int. J. Solids Struct. 46, 52–73.
Touhei, T., 2011. A fast volume integral equation method for elastic wave propagation in a half space. Int. J. Solids Struct. 48, 3194–3208.
Touhei, T., Kiuchi, T., Iwasaki, K., 2009. A fast volume integral equation method for the direct/inverse problem in elastic wave scattering phenomena. Int. J. Solids Struct. 46, 3860–3872.
Touhei, T., Hinago, T., Fukushiro, Y., 2014. Inverse scattering analysis of an elastic half-space by means of the fast volume integral equation method. Eng. Anal. Bound. Elem. 44, 130–142.